TDDFT from Molecules to Solids: The Role of Long-Range Interactions

FRANCESCO SOTTILE,[1,2†] FABIEN BRUNEVAL,[1] A. G. MARINOPOULOS,[1] L. K. DASH,[1] SILVANA BOTTI,[1] VALERIO OLEVANO,[1] NATHALIE VAST,[1] ANGEL RUBIO,[1,2] LUCIA REINING[1]

[1]*Laboratoire des Solides Irradiés, CNRS-CEA, École Polytechnique F-91128 Palaiseau, France*

[2]*Departamento de Física de Materiales, Facultad de Ciencias Químicas, Universidad del Pais Vasco, Centro Mixto CSIC-UPV/EHU and Donostia International Physics Center E-20018 San Sebastián/ Donostia, Basque Country, Spain*

Received 1 September 2004; accepted 2 December 2004
Published online 1 February 2005 in Wiley InterScience (www.interscience.wiley.com).
DOI 10.1002/qua.20486

ABSTRACT: Classical Hartree effects contribute substantially to the success of time-dependent density functional theory, especially in finite systems. Moreover, exchange-correlation contributions have an asymptotic Coulomb tail similar to the Hartree term, and turn out to be crucial in describing response properties of solids. In this work, we analyze in detail the role of the long-range part of the Coulomb potential in the dielectric response of finite and infinite systems, and elucidate its importance in distinguishing between optical and electron energy loss spectra (in the long wavelength limit $q \rightarrow 0$). We illustrate numerically and analytically how the imaginary part of the dielectric function and the loss function coincide for finite systems, and how they start to show differences as the distance between objects in an infinite array is decreased (which simulates the formation of a solid). We discuss calculations for the model case of a set of interacting and noninteracting beryllium atoms, as well as for various realistic systems, ranging from molecules to solids, and for complex systems, such as superlattices, nanotubes, nanowires, and nanoclusters. Int J Quantum Chem 102: 684–701, 2005

Correspondence to: L. Reining; e-mail: lucia.reining@polytechnique.fr

[†]Present address.

1. Introduction

Over the past decades we have witnessed a steady increase in the use of density functional theory (DFT) [1]. This holds not only for extended and relatively homogeneous systems, for which the initial, simplest approximations like the local density approximation (LDA) were originally designed; DFT is today also widely and successfully used to calculate ground-state properties of inhomogeneous systems and finite structures, like atoms or molecules, even maintaining the approximations on a relatively simple level. Concerning electronic excitations, the situation has evolved differently. DFT is a static ground-state theory, and the eigenvalues of the corresponding Kohn–Sham (KS) equation, or eigenvalue differences, are not meant to represent electron addition or removal energies, or transition energies, even when one disregards that approximations have to be made. For finite systems, eigenvalue differences can nevertheless be rather close to excitation energies. In fact, in the one-electron limit KS eigenvalue differences are identical to promotion energies. For more electrons, it is still true that the KS potential is better suited to describe neutral excitations than, e.g., the Hartree–Fock, because in KS occupied and unoccupied orbitals see the same potential and hence the same number of electrons [2]. Concerning other types of excitations, Chong et al. have shown that the orbital energies of occupied levels of atoms and molecules can be interpreted as approximate, but rather accurate, relaxed vertical removal energies [3].

One should also mention that in finite systems the problem of excitations well described by populating KS states of different symmetry can often be tackled by calculating total energy differences in a so-called Δ-self-consistent-field (Δ-SCF) scheme (see, e.g., Ref. [4]). However, the range of application of these schemes is limited. The problem can conceptually be solved by generalizing DFT to a time-dependent theory [5] (TDDFT). Now, the time-dependent KS potential can describe the response of the system to a time-dependent (as opposed to a static, as in DFT) local potential: This is the response measured in many spectroscopies creating electronic excitations, like absorption. First applications of TDDFT concerned finite systems [6], and were performed in the adiabatic local density approximation (TDLDA), with encouraging results. Subsequently, a large number of TDLDA calculations have been performed for atoms, molecules, and clusters (see Ref. [7] and references therein). Although the TDLDA shows shortcomings (e.g., it does not capture Rydberg series), it is able to describe a large class of finite systems, and systematically improves results with respect to the random phase approximation (RPA) [8], where exchange and correlation (xc) effects in the response are neglected. However, this statement is not true for extended systems. In fact, it has been found for simple semiconductors and insulators that absorption spectra calculated in TDLDA are generally very close to RPA ones, and result hence in significant disagreement with experiment. Note that the same is not true for electron energy loss spectra, which are often in reasonable agreement with experiment even on the RPA or TDLDA level.

In view of that situation, in order to obtain a deeper understanding, and to eventually improve the existing approximations for TDDFT, it is important to elucidate *which* are the features of finite versus infinite systems, and of absorption versus energy loss spectra, that determine such different behaviors.

As we discuss in this article, two key points for understanding this question are (i) the fact that states are localized in small molecules, whereas electrons are described as extended Bloch states in a solid, and (ii) the relative importance of long-range effects in a solid, compared to a finite system. Some discussion, especially of point (ii), has already been made (see, e.g., Ref. [7]). Here we analyze these questions more in detail. Starting from existing results, we add analytical and numerical calculations that show how the Coulomb interaction governs the transition between finite and infinite systems, and between absorption and energy loss spectra, as well as the transition between RPA and an improved TDDFT formalism. As a byproduct of our model calculations, we suggest a way to speed up the calculation of absorption spectra of molecules in the supercell scheme. We then give a series of examples of realistic systems, where the observed phenomena illustrate our discussions. To stress the *classical* origin of many of the effects, we compare to the outcome of effective medium theory, where appropriate.

Our article is organized as follows. In Section 2 we present the theoretical framework, adopting a formulation that puts absorption and loss functions on the same footing. These spectra are compared, and their behavior as a function of the distance between the objects composing the system is discussed analytically. We also give a brief reminder of

effective medium theory. Section 3 gives numerical results for model systems, in particular a model of interacting or noninteracting beryllium atoms. In Section 4 we present results of ab initio calculations for realistic systems: solids, superlattices, nanotubes, quantum wires, and clusters. Finally, we end with conclusions and perspectives. Unless otherwise indicated, we will use a compact notation for matrix products [namely in real space, $v\chi \equiv \int d\mathbf{r}' v(\mathbf{r_1} - \mathbf{r}')\chi(\mathbf{r}', \mathbf{r_2}, \omega)$ and similarly in reciprocal space] and Hartree atomic units throughout (i.e., $e^2 = \hbar = m_e = 1$).

2. Theory

Here we give a brief overview of both the ab initio and the classical effective medium approaches used to produce and discuss the results in the next sections.

A. RESPONSE FUNCTIONS IN TDDFT

Although we will not limit our target to infinite systems, we take the solid-state approach and describe all equations in reciprocal space. Keep in mind that we will perform later, whenever we wish to describe an isolated structure, the limit of the cell size going to ∞.[1] In this scheme, the *microscopic* dielectric function of a periodic system, which relates the total potential of the system to the external applied one, is given in terms of the bare Coulomb potential $v_{\mathbf{G}}(\mathbf{q})$ and the irreducible polarizability of the system $\tilde{\chi}_{\mathbf{G},\mathbf{G}'}(\mathbf{q}, \omega)$ by

$$\varepsilon_{\mathbf{G},\mathbf{G}'}(\mathbf{q}, \omega) = \delta_{\mathbf{G},\mathbf{G}'} - v_{\mathbf{G}}(\mathbf{q})\tilde{\chi}_{\mathbf{G},\mathbf{G}'}(\mathbf{q}, \omega). \quad (1)$$

Here $\mathbf{G}$ stands for a vector of the reciprocal lattice, and $\mathbf{q}$ is a vector in the first Brillouin zone. The polarization function $\tilde{\chi}$ includes, in principle, all many-body effects. However, it is most often evaluated within RPA [8], where xc effects in the response are neglected. $\tilde{\chi}$ has then simply the independent-particle (IP) form:

$$\tilde{\chi}(\mathbf{r}, \mathbf{r}', \omega) = \chi_0(\mathbf{r}, \mathbf{r}', \omega) = \sum_{ij} (f_i - f_j) \frac{\psi_i(\mathbf{r})\psi_j^*(\mathbf{r})\psi_j(\mathbf{r}')\psi_i^*(\mathbf{r}')}{\omega - \omega_{ij} + i\eta}. \quad (2)$$

Here $\omega_{ij} = (\epsilon_j - \epsilon_i)$, f_i are Fermi occupation numbers, and (i, j) label the states of energy ϵ_j and ϵ_i obtained from some equation for one-particle states. As usual, we take the energies ϵ_i and wave functions $\psi_i(\mathbf{r})$ to be solutions of the KS equation.

From the microscopic dielectric function, we have to obtain measurable quantities. In the case of absorption spectra, one calculates the imaginary part of the *macroscopic* dielectric function ε_{M}, which, according to the works of Adler and Wiser [8], can be obtained through

$$\varepsilon_{\mathrm{M}}(\omega) \equiv \lim_{\mathbf{q}\to 0} \frac{1}{[\varepsilon^{-1}(\mathbf{q}, \omega)]_{\mathbf{G}=\mathbf{G}'=0}}. \quad (3)$$

ε_{M} also allows one to obtain electron energy loss spectra (EELS) for vanishing momentum transfer, from the loss function $-\mathrm{Im}\{1/\varepsilon_{\mathrm{M}}\}$.

It is therefore obvious that EELS and absorption are closely related spectra, both carrying information about the electronic response of the system. At this point it is worth remembering that EELS is traditionally interpreted as being dominated by collective plasmon excitations, whereas single particle–hole excitations (essentially joint density-of-states) control the absorption spectra. This can be understood easily in the independent particle picture, since the imaginary part of the Fourier transform of (2) is proportional to $1/\omega^2 \, \Sigma_{v,c} \, |\langle\psi_v|\mathbf{v}|\psi_c\rangle|^2 \, \delta(\epsilon_c - \epsilon_v - \omega)$, where $\mathbf{v}$ is the velocity operator, and the sum runs over occupied (valence) and unoccupied (conduction) states ψ_v, ψ_c with energy ϵ_v and ϵ_c, respectively. Instead, because $-\mathrm{Im}\{1/\varepsilon_{\mathrm{M}}\} = \mathrm{Im}\{\varepsilon_{\mathrm{M}}\}/(\mathrm{Re}\{\varepsilon_{\mathrm{M}}\}^2 + \mathrm{Im}\{\varepsilon_{\mathrm{M}}\}^2)$, the structure in EELS is mainly given by regions where both the real and the imaginary part of ε_{M} are close to zero, that is, the classical condition for a collective (plasmon) mode [9].

Independently of the quality of the states ψ, the electronic excitations described by Eq. (2) are restricted to the generation of noninteracting particle–hole pairs. It is, however, important to recall that when the off-diagonal elements of $\varepsilon_{\mathbf{G},\mathbf{G}'}$ are properly accounted for in the matrix inversion (3)—in other words, when crystal local field effects (LFE) are taken into account—the formerly independent transitions do mix, leading to an effective "elec-

[1] In practice, one will perform the ab initio calculations for a finite cell size, even when one wishes to describe an isolated object. This influences the electronic structure and can lift degeneracies due to the imposed space group of the artificial crystal. Moreover, the induced potentials on the repeated objects influence the results. However, careful convergence tests allow one to reach the limit of the isolated object within a desired precision.

tron–hole" interaction (also called electron–hole exchange [7]). These LFE reflect the fact that an inhomogeneous system exhibits an electronic response that is position-dependent (and not only distance-dependent). It is intuitively clear that such an effect will be the stronger the larger the inhomogeneity of the system. Because a finite object represents a strong inhomogeneity in the otherwise empty space (surface effect), it is to be expected that LFE are particularly important for those structures.

As mentioned above, besides comparing finite and infinite systems we wish to compare the quantities describing absorption and loss functions. As has been shown in Ref. [7], both spectra can be described by a *generalized spectrum* $A(\omega)$

$$A(\omega) \equiv -\mathrm{Im}\{\lim_{\mathbf{q}\to 0} v_0(\mathbf{q}) S_{\mathbf{G}=\mathbf{G}'=0}(\mathbf{q}, \omega)\}, \qquad (4)$$

where the long-range ($\mathbf{G} = 0$) part $v_0(\mathbf{q})$ of the Coulomb potential $v_{\mathbf{G}}(\mathbf{q})$ appears. In this equation the matrix S stands for a modified polarization function $\bar{\chi}$ in the case of absorption, and for the reducible response function χ for EELS. In the framework of TDDFT, these functions are obtained by solving a Dyson-like screening equation, where the full response functions are related to the independent-particle one via a kernel that contains a xc contribution f_{xc} (i.e., the functional derivative of the time-dependent KS xc potential v_{xc} with respect to the density), and a bare Coulomb contribution. Only the latter distinguishes χ and $\bar{\chi}$:

$$\begin{cases} \bar{\chi} = \chi_0 + \chi_0(\bar{v} + f_{\mathrm{xc}})\bar{\chi} \\ \chi = \chi_0 + \chi_0(v + f_{\mathrm{xc}})\chi. \end{cases} \qquad (5)$$

Moreover, χ (or $\bar{\chi}$) can be alternatively expressed in terms of the irreducible polarizability $\tilde{\chi}$:

$$\begin{cases} \bar{\chi} = \tilde{\chi} + \tilde{\chi}\bar{v}\bar{\chi} \\ \chi = \tilde{\chi} + \tilde{\chi}v\chi. \end{cases} \qquad (6)$$

The Coulomb kernel has to be taken with (v) or without ($\bar{v} = v - v_0$) its long-range ($\mathbf{G} = 0$) contribution in the case of electron energy loss and absorption, respectively. This apparently subtle difference is crucial for extended systems, whereas its contribution in finite systems should be vanishing. Instead, the term $\bar{v}$ expresses the LFE, as one can easily see in the RPA case ($f_{\mathrm{xc}} = 0$), where the first line of Eq. (5), neglecting $\bar{v}$, yields $\bar{\chi} = \chi_0$, i.e., the result without LFE. Also the xc effects can play an important role: In many cases v or $\bar{v}$ alone is not sufficient to obtain quantitative (for EELS) or even qualitative (for absorption) agreement between theory and experiment [7, 10].

Recently, a class of xc kernels has been proposed that turned out to be very efficient in the description of solids. They are directly derived from the Bethe–Salpeter equation of many-body perturbation theory. A parameter-free ab initio expression has been obtained in several different ways, always leading to the same formula [7, 10–13]. The results using this kernel in conjunction with a quasi-particle bandstructure are in excellent agreement with those of the Bethe–Salpeter equation, with a potentially reduced computational effort; still, the calculations are significantly more cumbersome than those in RPA or TDLDA. However, when proposing the ab initio expression in Ref. [10], some of us have also shown that already the asymptotic *static long-range* contribution (LRC) of the form

$$f_{\mathrm{xc}}^{\mathrm{LRC}}(\mathbf{r}, \mathbf{r}') = \frac{\alpha}{4\pi|\mathbf{r} - \mathbf{r}'|}, \qquad (7)$$

where α is a material dependent parameter, is sufficient to simulate the strong continuum exciton effect in the absorption spectrum and in the refraction index of bulk silicon when quasi-particle energies are used as a starting point. More recently, we have shown [14] that α can be obtained directly from the static dielectric constant, and that the resulting f_{xc} leads to excellent absorption spectra for many small- and medium-gap semiconductors. In other words, a total kernel $\bar{v} + \alpha v/4\pi = \alpha/4\pi v_0 + (1 + \alpha/4\pi)\bar{v}$, which simply rescales the Coulomb contribution of the RPA, is able to simulate the main many-body effects in the absorption spectra of semiconductors. Note that hence, in the case of absorption, the only long-range contribution stems from α, which explains its strong effect even though its weight has been shown to be relatively small ($\alpha/4\pi$ is typically smaller than 0.05) in the case of absorption. In the case of EELS, $v\alpha/4\pi$ is added to a long-range term v of weight 1, which explains why α has to be strongly increased to have a significant effect [14]. As some examples below will illustrate, the long-range term v_0 is a crucial quantity for the understanding of many of the failures and successes of TDDFT.

In summary, the long-range ($\mathbf{G} = 0$) contribution to the bare Coulomb potential v makes the difference between absorption and EELS of solids. Whenever this contribution is negligible both spectra

should hence be equivalent. [Note, however, that this statement is based on the fact that in the long-wavelength limit for the photon (dipole approximation) the transverse ε_{xx} response is identified with the longitudinal response $\varepsilon(q_x \to 0)$. For an increasing size of a nanostructure, one cannot suppose any longer that the wavelength of the light is infinite with respect to the size of the structure, and the measured absorption and EELS will be different.] The effect of the remaining term ($\bar{v}$) (describing LFE) is expected to yield a strong modification of the spectra in a finite system, whereas in a solid it will depend on details of the spatial distribution of the charge density. Also xc effects in TDDFT have a Coulomb-like contribution that is very important for the absorption spectrum of solids. Therefore, the following discussions concerning Coulomb contributions are also relevant for the understanding of exchange and correlation.

B. ABSORPTION VERSUS EELS

It is now instructive to illustrate the previous discussion for the simplest case when LFE are neglected, i.e., $\bar{v} = 0$. In this case $\bar{\chi} = \tilde{\chi}$ and $\chi = \tilde{\chi} + \tilde{\chi} v_0 \chi$, so that the description of both absorption and EELS is then given by

$$\mathrm{Abs}(\omega) = -v_0 \mathrm{Im}\{\bar{\chi}_{00}(\omega)\} = -v_0 \mathrm{Im}\{\tilde{\chi}_{00}(\omega)\}$$

$$\mathrm{EELS}(\omega) = -v_0 \mathrm{Im}\{\chi_{00}(\omega)\} = -v_0 \mathrm{Im}\left\{\frac{\tilde{\chi}_{00}(\omega)}{1 - v_0 \tilde{\chi}_{00}(\omega)}\right\}. \tag{8}$$

In this simplified case it is clear that χ and $\bar{\chi}$ are fundamentally different (χ is screened, but not $\bar{\chi}$), and that this is entirely due to the (in principle) tiny difference of the kernel in Eq. (6) discussed above. It is clear from Eqs. (6) and (8) that, if the long-range part is negligible, χ and $\bar{\chi}$ are the same, and so are the EELS and absorption spectra.

To make a comparison between absorption and EELS for both finite and infinite systems, we apply Eq. (8) to the case of a solid where the lattice parameter is increased, in order to go toward the limit of an isolated system. In doing this limit, we exploit the fact that $v_0 \tilde{\chi}_{00} \propto (1/\Omega)$ where Ω is the volume of the unit cell of the lattice. Thus the ratio between EELS and absorption given by Eq. (8) is

$$\frac{\mathrm{Abs}}{\mathrm{EELS}} = \left[1 + \frac{\alpha}{\Omega} + \frac{\beta}{\Omega^2}\right], \tag{9}$$

which clearly shows how absorption and EELS tend to give the same spectrum in an isolated system, when $\Omega \to \infty$. Here α and β are functions of the frequency and depend, of course, on the polarization function $\tilde{\chi}$.

Equation (8) can be generalized in a straightforward way to the case when LFE are fully included (see Appendix for the derivation). In this general case $\bar{\chi}$ replaces $\tilde{\chi}$ in Eq. (8), yielding:

$$\begin{cases} \mathrm{Abs} = -v_0 \mathrm{Im}\{\bar{\chi}_{00}\} \\ \mathrm{EELS} = -v_0 \mathrm{Im}\left\{\dfrac{\bar{\chi}_{00}}{1 - v_0 \bar{\chi}_{00}}\right\}. \end{cases} \tag{10}$$

It is clear that the limit behavior (9) still holds in an analogous way.

Up to now we have not specified the form of the polarization operator $\tilde{\chi}$, which in most cases is taken to be the independent RPA response function; but to obtain qualitative agreement with experiments it is needed to include a higher degree of sophistication (such as the inclusion of the electron–hole interaction, absent in RPA, either through the solution of the Bethe–Salpeter equation of many-body perturbation theory or within TDDFT with an appropriate f_{xc} kernel).

C. A SIMPLE "ONE-POLE MODEL"

Here we derive the frequency dependence of the functions α and β, appearing in Eq. (9) for the simplest case where only a single transition with frequency ω_0 dominates the response function. In this "one-pole model," the imaginary part of the dielectric function is given by a delta function in energy:

$$\mathrm{Im}\{\varepsilon\} = \mathrm{Im}\{1 - v_0 \tilde{\chi}_{00}\} = \frac{v_0 A}{\Omega}[\delta(\omega - \omega_0) + \delta(\omega + \omega_0)], \tag{11}$$

and the corresponding real part is, by Kramers-Kronig:

$$\mathrm{Re}\{\varepsilon(\omega)\} = 1 - \frac{2 v_0 A}{\pi \Omega} \frac{\omega_0}{\omega^2 - \omega_0^2}. \tag{12}$$

From this we can evaluate the ratio between absorption and EELS, as in Eq. (9):

$$\frac{\mathrm{Abs}(\omega)}{\mathrm{EELS}(\omega)} = 1 + \frac{1}{\Omega}\left(\frac{4v_0 A\omega_0}{\pi(\omega^2-\omega_0^2)}\right) + \frac{1}{\Omega^2}\left[v_0^2A^2 \times \left(\frac{4\omega_0^2}{\pi^2(\omega^2-\omega_0^2)^2} + [\delta(\omega-\omega_0)+\delta(\omega+\omega_0)]^2\right)\right]. \quad (13)$$

Comparing with Eq. (9), we can infer the frequency dependence of $\alpha(\omega)$ and $\beta(\omega)$ for this model. We note from (12) that $\mathrm{Re}\{\varepsilon\}$ crosses the frequency axis when

$$\omega = \pm\sqrt{\omega_0^2 + \frac{2v_0 A\omega_0}{\pi\Omega}},$$

showing that the plasmon peak corresponding to $\mathrm{Re}\{\varepsilon\} = 0$ moves toward the given absorption peak at ω_0, as the cell volume Ω increases.

D. EFFECTIVE MEDIUM THEORY

To disentangle the different effects involved in the connection from solids to isolated structure, a fully classical picture might help. It provides analytical formulas that already take into account many of the effects we are considering. Effective medium theory (EMT) was originally developed to describe the dielectric properties of alloys containing clusters of different metals embedded in a matrix made of another metal [15]. Nowadays, EMT is extensively used to deal with photonic crystals and nanoscaled heterostructures. This classical approach is simply based on Maxwell's equations and on the further assumption that the dielectric response of the materials inside each constituent of the composite is the same as the one of bulk materials:

$$\varepsilon(\mathbf{r},\omega) = \varepsilon_i(\omega) \quad \text{if } \mathbf{r} \in \text{material } i, \quad (14)$$

where $\varepsilon_i(\omega)$ is the dielectric function of the bulk material labeled i. This assumption should be well justified when the size of the domains is large, i.e., when quantum effects due to the surface become negligible. EMT is a mesoscopic scale approach: It totally neglects the microscopic scale details, such as atoms and bonds, but correctly handles larger structures, such as interfaces, that are still small with respect to the wavelength of light. Although this scheme makes use of a local dielectric function $\varepsilon(\mathbf{r})$, it contains all the ingredients necessary to give a full account for the classical LFE arising from the presence of interfaces between domains.

As an illustration, consider a regular lattice of objects of dimensionality d made of material 1 embedded in a matrix of material 2 with a filling factor f (defined as the ratio of the object's volume over the total volume), in the limit case where f is small. The well-known Maxwell-Garnett formulas [15] can be derived under these assumptions, for every dimensionality d ($d = 0$ for dots, $d = 1$ for wires, $d = 2$ for slabs) and for both directions of the polarization of light (only $\perp$ direction is meaningful for $d = 0$):

$$\varepsilon_{\mathrm{M}}^{\parallel}(\omega) = f\varepsilon_1(\omega) + (1-f)\varepsilon_2(\omega) \quad (15)$$

$$\varepsilon_{\mathrm{M}}^{\perp}(\omega) = \varepsilon_2(\omega)\left(1 + \frac{(3-d)f\alpha(\omega)}{1-f\alpha(\omega)}\right), \quad (16)$$

where $\alpha(\omega) = (\varepsilon_1(\omega) - \varepsilon_2(\omega))/(\varepsilon_1(\omega) + (2-d)\varepsilon_2(\omega))$. $\varepsilon_{\mathrm{M}}^{\parallel}$ stands for the macroscopic dielectric function for light having polarization parallel to the interfaces and $\varepsilon_{\mathrm{M}}^{\perp}(\omega)$ for the macroscopic dielectric function for light having polarization perpendicular to the interfaces. Note that $\varepsilon_{\mathrm{M}}^{\parallel}$ is merely a weighted average of bulk dielectric functions, whereas $\varepsilon_{\mathrm{M}}^{\perp}(\omega)$ includes more intricate quantities related to the geometry, that account for classical LFE.

Expressions (15) and (16) provide, as a byproduct, the general result for the absorption spectra of isolated dots, wires, or slabs. If one increases the volume in which each single structure is embedded and one takes $\varepsilon_2 = 1$ for the vacuum, Eqs. (15) and (16) yield

$$\mathrm{Im}\{\varepsilon_{\mathrm{M}}^{\parallel}(\omega)\} \propto \mathrm{Im}\{\varepsilon_1(\omega)\} \quad (17)$$

$$\mathrm{Im}\{\varepsilon_{\mathrm{M}}^{\perp}(\omega)\} \propto -(3-d)^2\mathrm{Im}\left\{\frac{1}{\varepsilon_1 + (2-d)}\right\}. \quad (18)$$

Figure 1 shows the drastic change in the absorption of light polarized perpendicularly to the interface because of the dimensionality. In particular, Eq. (18) points out that, even in a fully classical picture, the absorption of any isolated structure, as large as one desires, will never tend to the absorption spectrum of the bulk, but rather to a function closely related to the loss function of the bulk.[2] Finally, the EMT may be considered as an effective tool to evaluate easily the dielectric properties of

[2]Of course, when one measures "bulk" absorption spectra, the samples are always finite. As mentioned above, the discussions here do not apply to the actually measured spectra of large samples, since then the wavelength of light can no longer be considered to be large compared to the sample size.

large-scale isolated structures, starting from the ones of the bulk constituents, since the most significant effects, i.e., the classical LFE, are properly handled. Evaluating Eqs. (15) and (16) for a given value of the filling factor f and comparing the result to the limiting case equations (17) and (18) allows one also to estimate the error made in ab initio calculations that use the artificial periodicity, provided that the unit cell is big enough to exclude that the ground-state electronic structure is still significantly changed by the presence of neighboring objects.

3. Illustrations: Model Systems

In this section we show numerical results to support the analytical conclusions of the previous section, with special attention to some results important from a practical point of view.

A. FROM SOLIDS TO MOLECULES

The first analysis concerns the infinite–finite system limit. We have performed numerical simulations of a fcc-periodic array of beryllium atoms with an increasing lattice parameter, in order to have atoms farther apart from each other, i.e., a periodic representation of an isolated system. We have used the standard supercell plane-wave representation of the electronic wave function for the ground-state electronic structure and the RPA for the response function,[3] i.e., $\tilde{\chi} = \chi_0$. Moreover, because we want to analyze the evolution of the spectra going toward a finite system, we sample the Brillouin zone only with the Γ point.

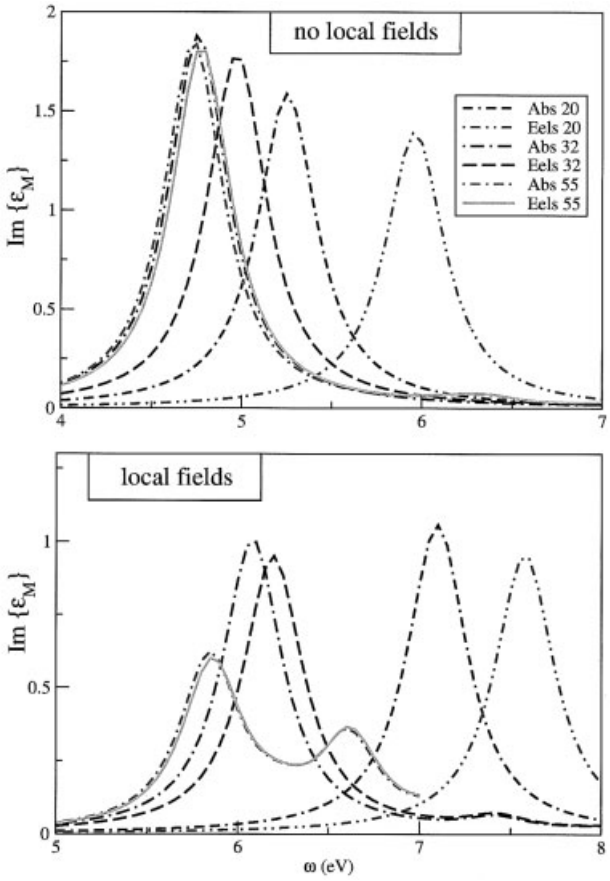

FIGURE 2. fcc array of beryllium atoms. Absorption and EELS for several cell sizes (i.e., for several interatomic distances): 20, 32, and 55 a.u. Upper panel: calculations made neglecting local fields. Bottom panel: local field effects included. The legend is the same for both panels.

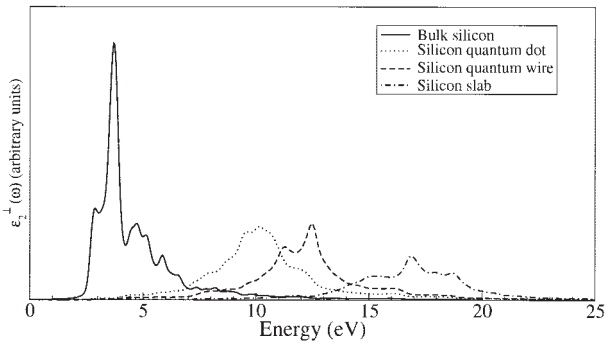

FIGURE 1. Model calculation of the absorption spectra of silicon isolated dots (dotted line), wires (dashed line), and slabs (dash-dotted line) for light polarized perpendicularly to the interface within EMT, compared to the RPA absorption spectrum of bulk silicon (solid line).

In the two panels of Figure 2 we show results for the fictitious solids formed by Be atoms at various interatomic distances. We clearly see that absorption and EELS become more and more similar as the cell size increases, both considering and neglecting LFE. In particular, for a cell with a lattice parameter of 55 a.u., in both cases the spectra almost coincide (the intensity of all the spectra of Fig. 2 has

[3]Inclusion of better exchange-correlation functionals will not modify the conclusions of the present analysis, which is based on the long-range part of the effective electron–electron potential.

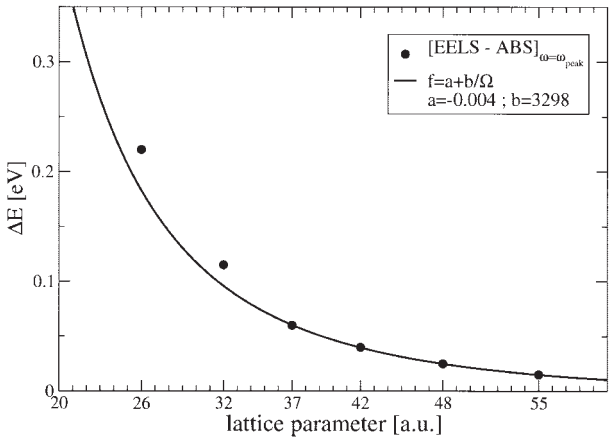

FIGURE 3. fcc array of beryllium atoms. Difference of peak positions of absorption and EELS as a function of the cell parameter. The extrapolation is represented by the full line.

been scaled by the factor $1/\Omega$, and Ω = volume of the unit cell).

Another fact that emerges from the calculations shown in Figure 2 is that the absorption spectrum converges much faster with cell size than the EELS one. This could be expected from the fact that the energy-loss spectrum is, by construction [see Eq. (8)], more sensitive to long-range effects, therefore larger size are needed to minimize interactions with neighboring cells. Consequently, for a given cell size the absolute error is expected to be smaller in a supercell calculation of $\mathrm{Im}\{\varepsilon_M\}$ rather than of the loss function. This provides us with a practical rule for the computation of spectra of finite-size structures. This finding is in perfect agreement with the analytical conclusions of Section II.B. We can make a more quantitative comparison between EELS and absorption by plotting the difference between the position of the first peak of both kind of spectra as a function of the cell size. This analysis is presented in Figure 3, together with the extrapolation to large cell volume of the analytical expression of Eq. (13). This extrapolation is done via a simple fitting function

$$f(\Omega) = a + \frac{b}{\Omega},$$

where f is the difference between the position of the absorption peak and the peak of the loss function. The parameters of the extrapolation appear in the legend and the fact that the asymptotic value $a = -0.004$ is very close to zero means a virtually perfect superposition of the peaks of absorption and EELS, in the limit of infinitely distant atoms, i.e., in the isolated atom limit. The good agreement of the fit gives further support to the analysis presented in Section 2.B.

When comparing the spectra with and without LFE in Figure 2, another important fact is observed. Without LFE the spectrum is dominated by a single peak related to a single bound-to-bound transition at about 5 eV, whereas with LFE there is a redistribution of oscillator strength toward higher energies and the formation of a double-hump structure. The blue-shift is a direct manifestation of the repulsive character of the Coulomb potential that renormalizes the original bound-to-bound transition mixing it up with other excitations. In fact, the peak position is moved from the discrete part of the spectrum toward the continuum.[4] Unfortunately, when the states are moved to the continuum we experience a more severe problem of convergence of the spectra with respect to cell size. This problem is a result of the nonproper description of continuum states in the supercell technique (confinement induced by the supercell).

B. FROM ABSORPTION TO ENERGY LOSS

We consider now a solid system. It is instructive to see the absorption and energy-loss spectra (within RPA and with LFE) for a real system, like silicon, in the same figure (Fig. 4). This figure shows the imaginary part of the response function [Eq. (5)] of bulk silicon, with a long-range contribution weighted by a variable α. The electronic structure calculations needed to construct χ_0 have been performed in DFT-LDA, at the lattice constant of 10.217 a.u. Following Eq. (4), the generalized spectrum $A(\omega)$ defines EELS or absorption depending if the long-range component v_0 has been included or not:

$$\left.\begin{matrix}\mathrm{Abs}\\ \mathrm{EELS}\end{matrix}\right\} = A(\omega) = -\mathrm{Im}\{v_0(\mathbf{q} \to 0)S_{00}(\mathbf{q} \to 0, \omega)\}, \tag{19}$$

with

$$S(\omega) = (1 - \chi_0\alpha v_0 - \chi_0\bar{v})^{-1}\chi_0. \tag{20}$$

[4]Exchange-correlation effects are attractive and give rise to an additional red-shift of the spectra. This is important to obtain quantitative description of the optical spectra of small clusters [7, 16–19].

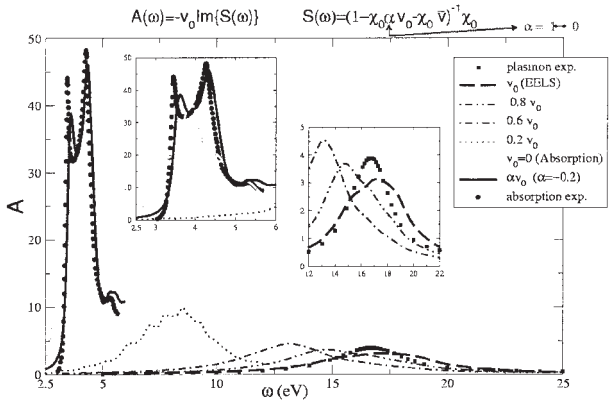

FIGURE 4. Bulk silicon. Continuous connection between EELS and absorption spectrum, via v_0. Experiments from Refs. [20] (absorption) and [21] (EELS).

If $\alpha = 1$, $A(\omega) =$ EELS, and if $\alpha = 0$, $A(\omega) =$ Abs. Moreover, we can follow in Figure 4 how the EELS turns into the absorption when v_0 is continuously switched off.

This simple example well illustrates the action of the long-range component, and how its inclusion or exclusion can make a big difference between absorption and electron energy loss spectra.

C. FROM RPA TO THE INCLUSION OF XC EFFECTS

Up to now, we have only analyzed the questions related to the microscopic and macroscopic contribution of the self-consistent variation of the Hartree potential. The latter turned out to be a key factor in determining the difference between absorption and EELS. We want now to discuss briefly another ingredient, which plays an important role in the description of practical spectra of materials, namely the exchange-correlation kernel f_{xc}. It was mentioned in Section 2, that an exchange-correlation kernel as $f_{xc} = \alpha/q^2$ is able to yield a good description of continuum exciton effects. The effect of this kernel can be seen in Figure 4. The most striking result is that the inclusion of the small *negative* ($\alpha = -0.2$) portion of v_0 in the total kernel leads to good agreement with the absorption experiment.[5] This result shows once again the importance of the long-range component of the Coulomb interaction in extended systems. In the case of the absorption, the αv_0 term is the only long-range term present, so that its inclusion is essential to describe correctly the strong continuum exciton in semiconductors like silicon.

[5]In this case, a scissor operator has also been applied to reproduce the self-energy contribution, and let the kernel take care only of the excitonic effects, as described in the previous section.

D. A JELLIUM MODEL: FROM CLUSTERS TO SOLIDS. LONGITUDINAL VERSUS TRANSVERSE RESPONSE

The evolution of the optical response of finite systems toward the bulk values offers the possibility to monitor the development of collective effects in metallic systems and to assess the similarities between the optical spectrum and EELS. The purpose of this section is to complement our previous discussion by looking at the size evolution of the optical absorption in the context of the simplest structural model of a spherical metallic cluster, namely the spherical jellium model. According to this model, the ionic background is smeared out to form a homogeneous distribution of positive charge $n_+ = n_e\Theta(R - r)$, where the radius R is related to the homogeneous bulk electron density by $(4/3)\pi R^3 = n_e$. Clusters of alkali elements turn out to be well described by this model [22, 23].

Within classical electrodynamics, an isolated metallic sphere in vacuum exhibits a series of multipolar surface plasmons of frequency ω_l [24] as a response to an arbitrary external electric field

$$\omega_l = \omega_p \sqrt{\frac{l}{2l+1}}, \tag{21}$$

where l is the angular momentum quantum number, and ω_p is the plasma frequency related to the "homogeneous" electron density n_e of the system given by $\omega_p = 4\pi n_e e^2/m_e$. For a dipolar field, the absorption is dominated by a single peak, the Mie surface plasmon with $\omega_M = \omega_p/\sqrt{3}$. Those surface modes are independent of the cluster size, in contrast to experiments, in simple metal clusters [22]. For large l the resonance frequency tends to the planar surface plasmon resonance $\omega_s = \omega_p/\sqrt{2}$. As we are interested in the evolution of the spectral features with system size, the full response

$$\alpha(\omega) = \int d^3r \int d^3r' V_{ext}(\mathbf{r};\omega)\chi(\mathbf{r},\mathbf{r}';\omega)V_{ext}(\mathbf{r}';\omega) \tag{22}$$

is not needed, and the knowledge of averaged quantities as the moments of the strength function $\{m_k = \int dE E^k S(E)$; called sum rules [25][6] with $S(E) = -1/\pi\ \mathrm{Im}\langle V_{\mathrm{ext}}\chi(\omega)V_{\mathrm{ext}}\rangle\}$ are enough to have a correct picture of the physical processes. In particular, for dipolar fields m_1 is model independent ($m_1 = (\hbar^2 e^2/2m)Z$, where Z is the number of electrons) and is connected with the well-known Thomas–Reiche–Kuhn (TRK) "f-sum" rule, whereas m_{-1} is connected to the static polarizability $\alpha = 2m_{-1}$. Moreover, if we now define mean energies as $E_k = (m_k/m_{k-2})^{1/2}$, then the average energy $\tilde{E}$ and variance σ of the absorption spectrum satisfies the following constraints: $E_1 < \tilde{E} < E_3$ and $\sigma^2 \leq (E_3^2 - E_1^2)/4$. For a uniform electronic spherical density (large R limit) and dipolar external field it is easy to show that $E_1 = E_3 = \hbar\omega_p/\sqrt{3}$. In this case, the spectrum is dominated by a single excitation that corresponds to the classical Mie plasmon described above, and illustrates the use of plasmon pole models.

Now we can go a step further and allow for a realistic description of the self-consistent electron charge density in the jellium model. In this case, we can show that

$$E_3 = \hbar w_p \sqrt{\frac{1}{3} - \frac{\delta Z}{3Z}}, \tag{23}$$

where $\delta Z = 4\pi \int_R^\infty r^2 n(r) dr$ measures the electronic spill-out beyond the positive background [23]. Equation (23) shows that E_3 tends toward the surface-dipole plasmon resonance $\omega_p/\sqrt{3}$ with increasing cluster size (hence, increasing Z), because $\delta Z/Z \to 0$ as $Z \to \infty$. All quantities involved are positive, hence E_3 reaches its limiting value from below. The inequality $\tilde{E} < E_3$ tells then immediately that E_1, as well as the average energy $\tilde{E}$, also approach $\omega_p/\sqrt{3}$ from below. This evolution of the optical dipole surface resonance toward the bulk-dipole value from below agrees with experiments for large K and Li clusters [26]. Similarly, in this model the static polarizability is enhanced with respect to the classical Mie value, due to the spill-out of the electronic density.

In the formal quantum mechanical framework discussed in the previous sections, the interaction between an electronic system and an external field, given by the potential $V_{\mathrm{ext}}(\mathbf{r}; t) = \int d\omega e^{-i\omega t} V_{\mathrm{ext}}(\mathbf{r}; \omega)$, can be fully described within linear response by knowing the imaginary part of the polarizability tensor (22), from which the photoabsorption cross section is proportional to the imaginary part of the dynamical polarizability, or equivalently to the imaginary part of χ. In other words, it is proportional to the imaginary part of an effective inverse longitudinal dielectric function $\varepsilon^{-1} = 1 + v\chi$. Following this approach, it seems evident that by increasing the system size toward the bulk limit we will reach the EELS spectra instead of the bulk optical absorption, as obtained in the simple jellium model discussed above. To reach this conclusion we have described the photon field in a longitudinal gauge, taking into account only electric-field effects. However, neglecting current-induced fields is only justified when the size of the system is smaller than the wavelength of the photon field, otherwise the absorption spectrum is characterized by the current–current response function (transverse) instead of the density–density response function that we have been using up to now.

Now it is important to make contact with the simple jellium model and note that bulk plasmons are longitudinal excitations that, in principle, cannot be probed by optical absorption but they can be seen by EELS. The distinction between longitudinal and transverse modes (surface and volume plasmons are pure transverse and longitudinal excitations, respectively) breaks down in low-dimensional structures, making those modes also accessible to light absorption experiments. In this context, we can envision that the optical absorption spectrum and EELS of finite systems would be proportional. However, as the size increases the distinction between longitudinal and transverse becomes relevant not only to make a distinction between the equation leading to the macroscopic function ε_{M} and loss function (see previous section), but also for the calculation of the matrix elements of the linear-response tensor χ where the proper longitudinal (EELS) and transverse (photon) external fields have to be considered.

It is relevant to discuss now the relation to EELS experiments. To do so it is better to write down the energy loss probability $P(\omega)$ corresponding to an electron with velocity v interacting with an isolated sphere of dielectric function $\varepsilon(\omega)$ [28] at a distance b (impact parameter). Integrating over the electron trajectory and neglecting retardation effects in the induced potential, the final result is

[6]For q- and l-dependent external fields ($j_l(qr)Y_{l0}(\Omega)$) represents the angular decomposition of an incident photon, described as a plane-wave $e^{i(\mathbf{qr}-\omega t)}$, the general expressions for the odd sum rules are given in Refs. [23, 27].

$$P(\omega) = \frac{4R}{\pi v^2} \sum_{l=1} \sum_{m=0}^{l} \frac{2 - \delta_{m0}}{(l+m)!(l-m)!} \times \left[\frac{\omega R}{v}\right]^{2l} K_m^2[\omega b/v]\mathrm{Im}\{\gamma_l(\omega)\}, \quad (24)$$

where $K_m(x)$ stand for the modified Bessel functions and $\gamma_l(\omega)$ is the sphere surface response given by

$$\gamma_l(\omega) = \frac{l(1-\varepsilon)}{l\varepsilon + l + 1}. \quad (25)$$

Equation (24) takes into account the contribution of all the multipolar terms of the induced potential created by the moving charge. Quantum mechanical effects are embodied in the otherwise isotropic dielectric response $\varepsilon(\omega)$ that can be obtained directly from χ. Again, the excitation frequencies are determined by the zeros of the denominator of γ_l and for a simple metal [described by a Drude-like dielectric response $\varepsilon(\omega) = 1 - \omega_p^2/\omega^2$] are given by the classical Mie multipolar plasmon frequencies ω_l [Eq. (21)]. Note that the dipolar term is dominant only when the sphere radius is much smaller than the range of variation of the field $R \ll v/\omega$ or when the probe electron travels far away from the target $b \gg R$. However, when the radii are of the order of v/ω_s many l-terms contribute, indeed, for large R the dipolar term becomes negligible as the probe sees a "nearly-flat" surface. This can be rationalized in terms of the image charge induced by an electron close to a large sphere. This induced density piles up in a small region close to the probe; thus many multipolar terms are needed to describe such a localized charge. In the usual case of a large impact parameter, the dipolar term becomes the dominant one in Eq. (24), and in this case we see that both EELS and the dipolar optical absorption spectra are proportional, as both are related to the imaginary part of χ in finite systems. This result corroborates the general discussion in this and the previous section and the results of our quantum mechanical calculations.

4. Illustrations: Real Systems

In this section we present applications to finite and strongly inhomogeneous systems that prove the importance of the inclusion of the $\bar{v}$ term, describing LFE.

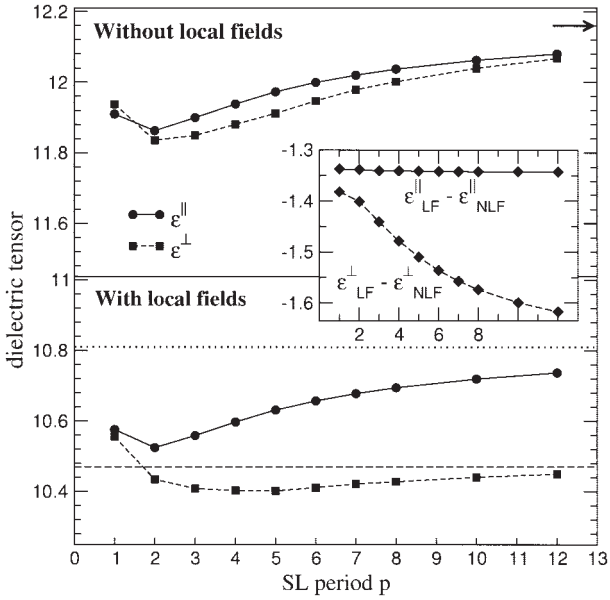

FIGURE 5. RPA static dielectric tensors of $(GaAs)_p/(AlAs)_p$ SLs calculated without (ε_M^{NLF}, upper panel) and with (ε_M^{LF}, lower panel) LFE and their difference, i.e., the LFE (inset), as a function of the SL period p from Ref. [29]. Arrow: average of bulk GaAs and AlAs dielectric constants, calculated without LFE. Dotted (dashed) line: classical effective medium value of $\varepsilon_M^{\parallel}$ ($\varepsilon_M^{\perp}$).

A. GAAS/ALAS SUPERLATTICES

Semiconductor superlattices (SLs) are multilayered structures artificially constructed by epitaxial growth techniques. They are an example of systems where the inhomogeneity is determined by the geometrical structure. As we already know that LFE measure the inhomogeneity of the charge density, their contribution is expected to be essential to describe such systems. Botti et al. [29, 30] studied the dielectric tensor of $(GaAs)_p/(AlAs)_p$ SLs, grown in the [001] direction. GaAs and AlAs have both zinc-blende structures with almost the same lattice parameter a. In the SL, the reduction of the originally cubic symmetry gives rise to a dielectric anisotropy, which depends in a nontrivial way on the layer width pa, where p is the number of planes constituting each layer. The possibility to control the anisotropy of the dielectric function (i.e., the birefringence) through the manufacturing of these materials has been successfully exploited to generate optical frequency conversion in the low-frequency region [31]. To this purpose, it is interesting to study the zero frequency limit of the birefringence.

Figure 5 shows the static dielectric function for

light polarized in the plane of the interface $\varepsilon_M^{\parallel}$ and in the direction perpendicular to the interface $\varepsilon_M^{\perp}$, as a function of the SL period p. The curves in the upper panel of Figure 5 refer to independent-particle (IP) RPA calculations, which neglect LFE. The differences between $\varepsilon_M^{\parallel}$ and $\varepsilon_M^{\perp}$ are due to quantum-confinement effects. For large layer widths, quantum-confinement effects vanish and $\varepsilon_M^{\parallel}$ and $\varepsilon_M^{\perp}$ tend to the average of the bulk dielectric constants of GaAs and AlAs calculated without LFE (arrow on the upper panel of Fig. 5). As a consequence, the calculated birefringence $\Delta n = \sqrt{\varepsilon_M^{\parallel}} - \sqrt{\varepsilon_M^{\perp}}$ goes to zero. This theoretical prediction is completely misleading, as a vanishing birefringence is not only in disagreement with experimental data, but also with the classical limit given by effective medium theory (Section 2.D).

The lower panel of Figure 5 shows the dielectric tensor components calculated including LFE. The LFE are displayed in the inset of Figure 5: For an in-plane light polarization, they are found to be almost constant with the period; in particular, they are equal to the average of LFE corrections to the dielectric constants of bulk GaAs and AlAs. This is consistent with the fact that the multilayer structure is not "seen" in plane. On the other hand, for increasing p, LFE give increasingly negative contributions in the direction that crosses the interfaces, where the inhomogeneity of the medium is brought into play. Thanks to the anisotropy of LFE, the birefringence undergoes a steep rise in the small–medium period region, reaching a finite plateau value for large SL periods, in agreement both with the experimental data [32] and the classical effective medium theory.

B. GRAPHITE/GRAPHENE AND CARBON NANOTUBES

Carbon structures are a much studied subject, not only because of technological importance, but also because they can be used as prototypical illustrations in many circumstances. For our purpose, the interesting feature is that carbon structures cover all dimension ranges, from the 3D bulk diamond, quasi-2D graphite, quasi-1D nanotubes to small fullerene-like objects. According to the dimension and feature studied, different effects can be important. When one studies EELS in bulk diamond, for small momentum transfer bandstructure effects are dominant whereas other contributions, in particular LFE, can be neglected [33]. When the dimension is reduced and hence the system becomes less isotropic and/or less homogeneous, other effects start to be important. For example, recent RPA calculations for graphite and other graphene-layer structures showed that the interlayer interaction was the cause of considerable changes to the energy-loss function in the small-q momentum-transfer limit [34]. Figure 6 contains the RPA results for the dielectric and energy-loss functions of AB graphite and of a number of graphene geometries. The latter have been obtained by increasing the layer–layer separation, thereby effectively increasing the magnitude of the ratio $(c/a)_{hex}$ of the lattice parameters and, therefore, the unit-cell volume.

It can be seen (Fig. 6) that in the loss function two distinct peaks appear at certain frequencies, depending upon $(c/a)_{hex}$. These peaks represent the longitudinal collective excitations of the valence electrons, namely the plasmons. For graphite and graphene (where the valence electrons are of the π and σ type) these plasmons are known as the π and the $\pi + \sigma$ (total one). On the other hand, the in-plane absorption spectrum, $\mathrm{Im}\{\varepsilon_M\}$, displayed in

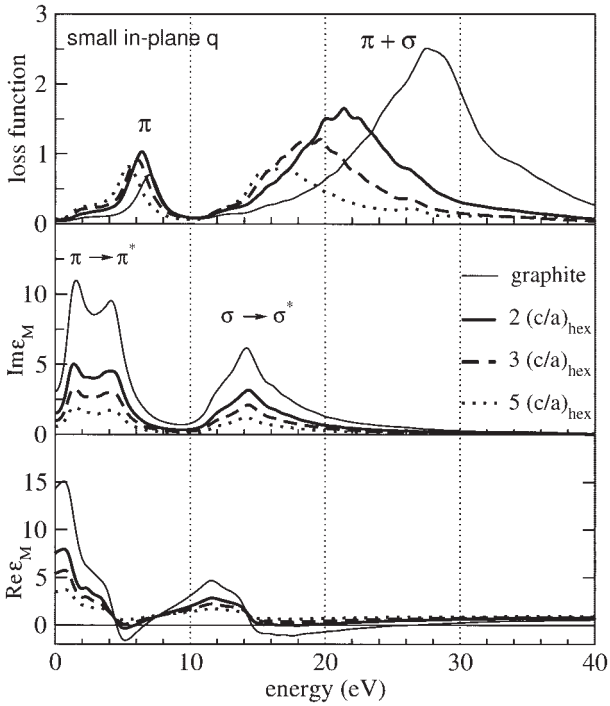

FIGURE 6. Energy-loss and dielectric function for small in-plane **q** (=0.22 Å^{-1}) for graphite and the graphene-layer geometries with multiple $(c/a)_{hex}$ ratios. The results shown were obtained within the RPA without LFE. LFE are negligible in this **q** range.

the middle panel in Figure 6, is dominated by a very intense peak structure at low frequencies (up to 5 eV) and also by another peak structure of broader frequency range that sets in beyond 10 eV and has a pronounced peak at 14 eV. The origin of these peak structures is due to $\pi \rightarrow \pi^*$ and $\sigma \rightarrow \sigma^*$ interband transitions, respectively. It is evident that the frequency range of these transitions and the position of the major absorption peaks do not change for different $(c/a)_{\text{hex}}$. Only a uniform decrease in oscillator strength is seen owing to the larger unit-cell volumes when increasing the $(c/a)_{\text{hex}}$ ratio. This stability of the absorption with interlayer distance has been explained in terms of the interband transitions involving electron states at specific regions of the Brillouin zones [34].

In contrast, the loss function exhibits more important interaction effects: in particular the peak position of the total $(\pi + \sigma)$ plasmon is extremely sensitive to variations of the interlayer distance, i.e., the $(c/a)_{\text{hex}}$ ratio. The tendency observed is that for larger $(c/a)_{\text{hex}}$ the macroscopic screening vanishes $(\text{Re}\{\varepsilon_{\text{M}}\} \rightarrow 1)$ and the loss and absorption functions tend to coincide: $-\text{Im}\{1/\varepsilon_{\text{M}}\} \rightarrow \text{Im}\{\varepsilon_{\text{M}}\}$. This coincidence is achieved mainly through the displacement of the $\pi + \sigma$ plasmon: this plasmon is displaced at a much faster rate to lower frequencies, toward the 14-eV peak of the absorption spectrum (peak of the $\sigma \rightarrow \sigma^*$ transitions), with increasing $(c/a)_{\text{hex}}$. In contrast, the π-plasmon peak position remains insensitive to changes of $(c/a)_{\text{hex}}$ since this plasmon is already located very close to the 0–5-eV range of the $\pi \rightarrow \pi^*$ transitions in $\text{Im}\{\varepsilon_{\text{M}}\}$.

Having, up to now, discussed the interaction effects in graphite and graphene it is instructive to examine the significance of these effects in structurally related materials: the carbon nanotubes. Here we are concerned with the single-walled tubes arranged in two distinct configurations: in the solid as a crystalline hexagonal phase but also as nearly isolated (distant) objects with very weak intertube interaction in the ground state.

Experimentally, the analysis of the observed energy-loss data of crystalline samples of single-walled carbon nanotubes is hindered by the fact that the samples studied contain tubes non-perfectly aligned and of a range of diameters [35]. The issue of intertube interaction is also extremely essential since recently it became possible to grow well-aligned carbon tubes of specified diameter (~4 Å) inside the channels of zeolite matrices [36]; therefore the intertube spacings depend upon the structural characteristics of the host material in the experiment.

In particular, the very thin armchair (3, 3) nanotubes of nearly 4-Å diameter have been the subject of a number of recent theoretical studies, focusing on their dielectric response in the energy range of valence–electron excitations (see Refs. [37, 38]). RPA calculations of the optical absorption including LFE revealed a striking manifestation of intertube interaction effects: owing to the depolarization, for the case of widely separated nanotubes [37], the nanotube system did not absorb the incident light (for frequencies up to 4 eV) when the latter was polarized normal to the tubes axes, a phenomenon initially observed in the experiment [36].

For these (3, 3) single-walled nanotubes we determined the electron energy-loss function for $\mathbf{q}$ orientations parallel to the tubes axes. For the case of small $\mathbf{q}$ (0.23 Å^{-1}) the loss function is plotted in Fig. 7(a) for two chosen intertube (interwall) separations: in the first geometry (distant tubes) the intertube distance is set at 5.5 Å, whereas in the second geometry we are dealing with a solid of strongly interacting tubes. In the latter case, the total energy minimization yielded an intertube distance of 3.2 Å. It can be seen that three distinct peaks appear at certain frequencies in the loss functions. The low-frequency intraband plasmon is first seen at ~2 eV (denoted as i). This plasmon originates from the free carriers of the two linear bands that intersect at the Fermi level (a situation common to all armchair carbon tubes [39]). Rather close in energy is found the π plasmon (~5 eV). The peak frequencies of these two plasmons are the same for both intertube distances studied here. Finally, the total $(\pi + \sigma)$ plasmon is found beyond 20 eV with a peak frequency depending strongly upon the intertube distance: the strong intertube interaction in the solid yields a shift in the $\pi + \sigma$ plasmon peak by almost 6 eV with respect to the peak of the same plasmon for the distant tubes.

For the large q considered here [0.76 Å^{-1}; see Fig. 7(b)] both π and $\pi + \sigma$ plasmons disperse toward higher frequencies. For this large-q magnitude, the intraband plasmon completely disappears and the π plasmon is heavily damped. The LFE are now very important especially for the system of distant tubes: LFE cause a considerable blue-shift of the center of gravity of the $\pi + \sigma$ plasmon. As a result this plasmon-peak position for the distant tubes approaches the position of the same plasmon in the

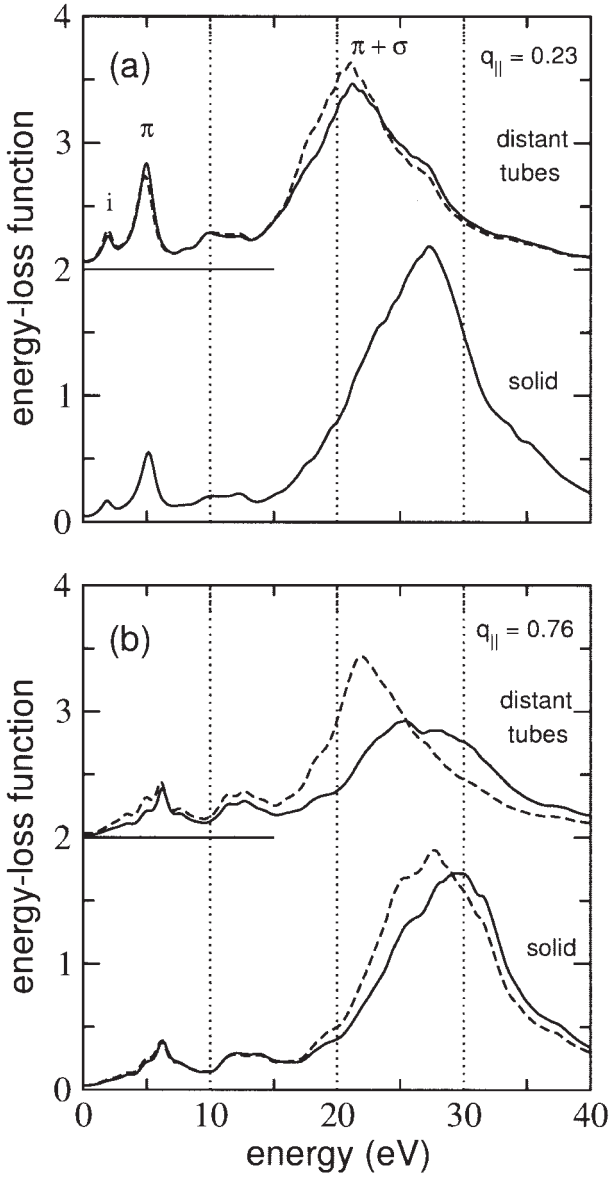

FIGURE 7. Calculated RPA energy-loss functions for the distant (3, 3) tubes and the solid of (3, 3) tubes. The results were obtained for two different magnitudes of momentum transfer $\mathbf{q}_{\|}$: (*a*) *equal to* 0.23 $Å^{-1}$ *and* (*b*) 0.76 $Å^{-1}$. $\mathbf{q}_{\|}$ is parallel to the tubes axes. Continuous (dashed) curves denote results obtained with (without) LFE in the response.

solid. In lower frequencies LFE do not appear as important.

The fact that the peak frequency of the $\pi + \sigma$ plasmon is governed by the intertube distance resembles closely the situation in graphite and graphene where the same plasmon displays a similar dependence upon the interlayer distances, for small magnitudes of q. To a good approximation, the $\pi + \sigma$ plasmon peaks in the (3, 3) nanotubes, in the solid and for the distant ones, (for small **q** parallel to the tubes' axes) are very close to the peak positions of this plasmon in graphite and graphene [for 2 $(c/a)_{\text{hex}}$] for in-layer **q** orientations (see Fig. 6). On the other hand, the lower-frequency part of the loss function of the tubes shows certain important differences from the graphitic one. Graphite does not support a low-frequency intraband plasmon in the 1–2-eV range; also the graphitic π plasmon has a higher peak frequency (at ~7 eV) for small in-layer **q** (Fig. 6). This suggests that the different details in the electronic bandstructures between graphite and the (3, 3) carbon tubes play a more essential role in this energy range.

The present results demonstrate that both the intertube Coulomb interaction and LFE (whose strength depends on intertube distance as well as the magnitude of q) are important factors that influence most notably the peak position of the total plasmon in the loss function. The lower part of the loss function exhibits a much weaker dependence upon the intertube distances.

C. SILICON NANOWIRES

An interesting example of a unidimensional material is a single quantum wire of silicon with bonds saturated by hydrogens. Because this wire is made of simple materials, silicon and hydrogen, the complexity of the system only arises from its geometry, which yields quantum confinement in two directions, band folding and charge inhomogeneities. As in the case of SLs, the LFE are expected to be large for a direction of polarization of the light crossing the interfaces.

Here we simulate distant [110] wires with a supercell technique. Each cell contains a $Si_{16}H_{12}$ unit, whose diameter is about d = 12 Å. The interwire distance, 15 Å, is large enough to make wires practically isolated. After structural relaxation within LDA, we performed a TDDFT calculation of the dielectric function within RPA with and without LFE. Alternatively, the EMT was used through Eqs. (15) and (16) with $f = 0.10$ to evaluate the dielectric function of the heterostructure from the one of bulk silicon. The imaginary part of the dielectric function within the different approaches is reported in Figure 8. For light polarized along the axis, the LFE in $\varepsilon_2^{\|}$ are very small (dark solid and dashed lines). As the polarization of light does not cross any interface, the inhomogeneity of the nanostructure is not

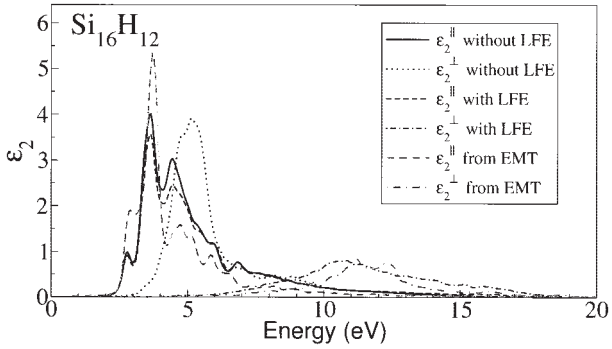

FIGURE 8. Imaginary part of the dielectric functions of [110] $d = 12$ Å silicon hydrogenated nanowires, calculated within RPA with or without LFE, and within EMT for both polarizations of light.

experienced and, as a consequence, LFE are not larger here than in the bulk material. On the contrary, for light polarized perpendicularly to the axis, the LFE on $\varepsilon_2^{\perp}$ are huge. Similarly to the case of carbon nanotubes [37], the depolarization effects due to LFE make the wire transparent up to about 5 eV (dark dash-dotted line). If the LFE were neglected (dark dotted line), the conclusion would have been completely different, with qualitatively wrong dielectric properties.

A striking conclusion provided by these results is that the classical LFE taken into account thanks to EMT (lighter lines) yield very good results with respect to a full, computationally more expensive RPA calculation. This means that, even in so small nanostructures, quantum effects due to interfaces are small compared to the overall bulklike behavior. For instance, it can be noticed that peaks of $\varepsilon_2^{\parallel}$ are located closely to the peaks of the bulk (given by the EMT in that direction; lighter dashed line). The major effect of the interfaces hence lies in the depolarization charges on the wire surface, which are properly treated already within a classical picture.

D. SILICON NANOCLUSTERS

Silicon nanocrystals in the form of spherical quantum dots have been widely investigated in the past decade [16, 40–43] to explain how the photoluminescence of porous silicon is related to quantum confinement and to surface passivation. Despite the large number of studies, many open questions still exist, mainly because of the disagreement of the results of calculations performed within different theoretical approaches [42].

Important effects on the peak positions are found as expected, in dependence on the cluster size. As a general rule, when the cluster size decreases the increase in the quasi-particle gap blue-shifts the absorption edge. The increase in the excitonic binding energy partially counterbalances this shift. Both effects have to be adequately accounted for, in order to obtain an accurate description of the optical spectra. This means that the TDDFT xc kernel must contain the sum of the physics of quasi-particle energies corrections and electron–hole binding. It has been shown that TDLDA xc kernel usually provides good agreement with experiments for the excitation energies of semiconducting clusters [16, 42, 44].

We present here optical absorption spectra of hydrogen passivated silicon nanocrystals, obtained using TDDFT within both the RPA and the TDLDA. We studied nanocrystals with a diameter up to 10 Å, whose initial geometry was obtained by cutting a spherical portion of the perfect fcc crystal. Dangling bonds were saturated with hydrogen atoms oriented in the directions of the missing bonds and a structural relaxation of the cluster was performed before calculating the optical response at zero temperature and fixed geometry. Figure 9 shows the results for the absorption spectra of Si_5H_{12} and $Si_{10}H_{16}$ nanocrystals. The dashed lines refer to the independent particle (IP) RPA calculations, where

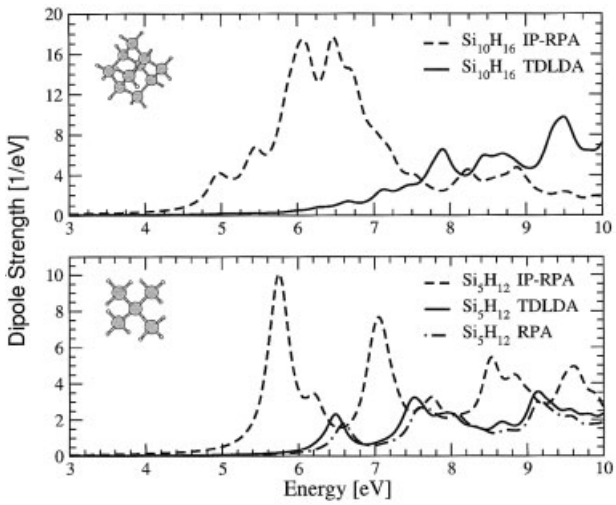

FIGURE 9. Calculated averaged dipole strength for $Si_{10}H_{16}$ (upper panel) and Si_5H_{12} (lower panel) clusters, obtained within IP-RPA (dashed line), within TDLDA (solid line), and within RPA (dot-dashed line). The geometrical structure of the relaxed nanocrystal is also shown.

both the xc kernel and the local fields are set to zero. The IP-RPA curves exhibit prominent peaks in a low-energy region (4–6 eV), where TDLDA calculations (solid lines) predict instead that the system must be transparent. In fact, in TDLDA calculations the absorption edge is moved to higher energies, in agreement with experimental findings. We note that the RPA curve is always found to be extremely close to the TDLDA curve (as shown for the case of Si_5H_{12} by the dot-dashed line in the lower panel of Fig. 9). This proves that the main contribution comes from classical crystal LFE rather than from xc effects.

Observe that silicon nanocrystals are a model system for a regular lattice of objects of dimensionality 0 in an empty space. The drastic change in the absorption of one isolated cluster with respect to bulk silicon is actually still verified in nanocrystals much bigger than the ones we studied (see, for example, the TDLDA absorption spectrum of the $Si_{147}H_{100}$ cluster in Ref. [16]). In Ref. [16], Vasiliev et al. show that as the size of the cluster increases, the absorption edge gradually decreases, and the discrete spectra for small clusters evolve into continuous spectra for large clusters. This trend is also confirmed by our present calculations for clusters with a diameter smaller than 10 Å. In analogy to what happens in quantum wires, and coherently with the effective medium limit (see Section 2.D), the absorption spectrum does not seem to approach the absorption spectrum of bulk silicon, but rather a function closely related to the loss function of silicon.

E. ELECTRONIC EXCITATIONS FROM SEMICORE STATES IN ZrO_2 AND TiO_2

We finally illustrate the drastic effect of the crystal LFE on the excitation from semicore levels in monoclinic zirconia (ZrO_2) [45] and rutile (TiO_2) [46]. In the atom, these states are located deep in energy, but have a high spatial overlap with the 4d (resp. 3d) states. In the solid, these states are located at 25 eV (in ZrO_2) or 32 eV (in TiO_2) below the top of the valence band. Their excitation gives rise to plasmons in the 30–60-eV range—the $N_{2,3}$ edge in ZrO_2 or the $M_{2,3}$ edge in TiO_2. The RPA spectra without LFE, shown in the inserts of Figures 10 and 11 (dashed line), compare reasonably well with the experimental data (solid line) up to 30 eV in ZrO_2 (resp. 40 eV in TiO_2). These peaks correspond to excitation from extended states, the valence plasmon around 15 eV and the collective excitation stemming from the oxygen 2s states. However, at higher energy it becomes necessary to include crystal LFE, as illustrated in Figures 10 and 11. This

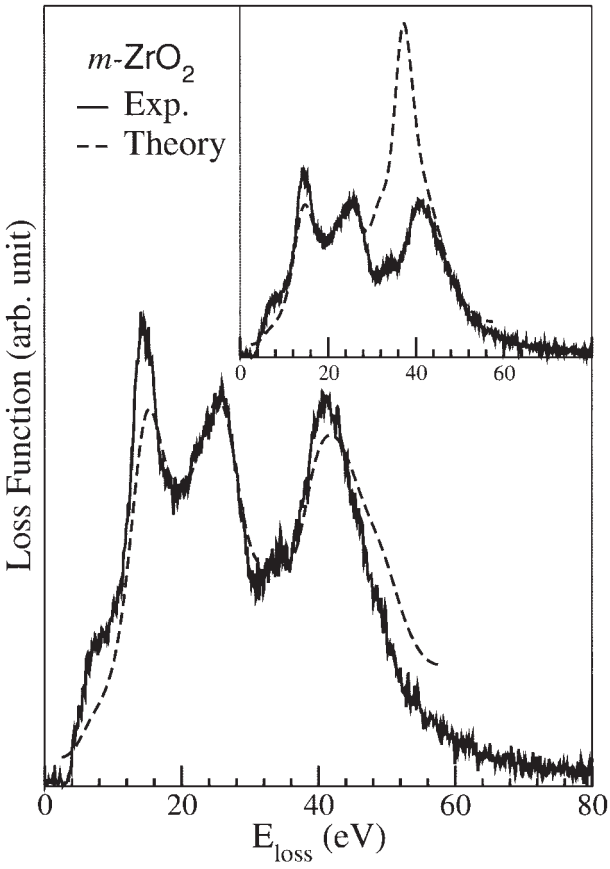

FIGURE 10. Loss function for monoclinic zirconia. Solid line: experiment. Dashed line: theory with LFE. Inset: theory without LFE. The theoretical curves have been convoluted with a Voigt profile: Gaussian of HWHM of 1 eV, and Lorentzian function of HWHM of 1 eV.

results in the calculated main 4p plasmon being shifted towards higher energies by ~5 eV in both ZrO_2 and TiO_2, in agreement with experiment. This effect also manifests itself in the electron energy loss spectra of other transition metal oxides, for example, NiO [47].

5. Conclusions

We have discussed the importance of Coulomb contributions to the electronic spectra. In particular, besides a discussion of the impact of crystal local field effects in finite systems, we have shown the importance of the long-range part, which governs the difference between absorption and loss spectra, in extended systems. The long-range component

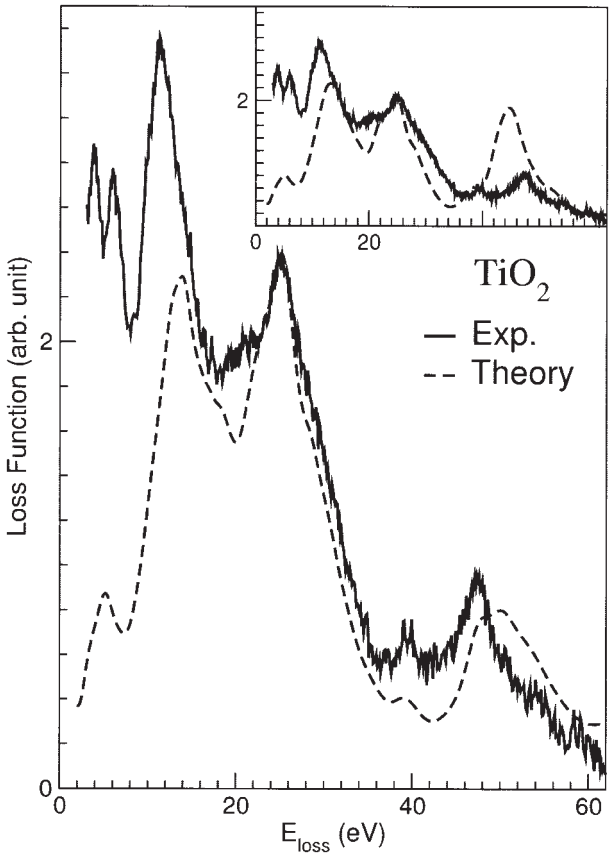

FIGURE 11. Loss function for rutile. Solid line: experiment. Dashed line: theory with LFE. Inset: theory without LFE.

leads to strong interactions in the excited state that are not present in the ground state. We have performed model calculations that illustrate the relation between finite and infinite systems, and between absorption and loss spectra. We have then presented results for the static response of superlattices, the EELS of graphite, carbon nanotubes, and transition metal oxides, the absorption spectra of silicon quantum wires and of hydrogenated silicon clusters, in order to stress the importance of these effects in realistic situations. Even for the cases where we have limited ourselves to RPA calculations, the results presented here are also important for the discussion of exchange-correlation effects, since the latter contain similar terms that describe excitonic effects.

ACKNOWLEDGMENTS

This work was funded in part by the EU's RTN NANOPHASE, the EU's 6th Framework Programme through the NANOQUANTA Network of Excellence (NMP4-CT-2004-500198), the French "Ministère de la recherche" in the framework of the "ACI Nanostructures," Spanish DGES, Basque Country University, and Iberdrola S.A. The work of L. K. D. was funded by the joint research program "ISMIR" between CEA and CNRS. Calculations have been done using ABINIT (http://www.abinit.org/), PWSCF (http://www.pwscf.org/), LSI-CP, and LSI-DP (http://theory.polytechnique.fr/codes/). Computer time was granted by IDRIS (project 000544) and by CEA/DSM on the cluster of Compaq Alphaserver (project p543) and NEC SX6 (project p93). A. R. acknowledges support from the Salvador Madariaga program of the Ministry of Science and Education of Spain for a sabbatical leave at the Ecole Polytechnique where this work was started.

References

1. Hohenberg, P.; Kohn, W. Phys Rev 1964, 136, B864; Kohn, W.; Sham, L. J. Phys Rev 1965, 140, A1133.
2. Savin, A.; Umrigar, C. J.; Gonze, X. Chem Phys Lett 1998, 288, 391; Casida, M. E.; Salahub, D. R. J Chem Phys 2000, 113, 8918; Hamel, S.; Casida, M. E.; Salahub, D. R. J Chem Phys 2002, 116, 8276.
3. Chong, D. P.; Gritsenko, O. V.; Baerends, E. J. J Chem Phys 2002, 116, 1760.
4. Jones, R. O.; Gunnarsson, O. Rev Mod Phys 1989, 61, 689.
5. Runge, E.; Gross, E. K. U. Phys Rev Lett 1984, 52, 997; Gross, E. K. U.; Kohn, W. Phys Rev Lett 1985, 55, 2850.
6. Zangwill, A.; Soven, P. Phys Rev A 1980, 21, 1561.
7. Onida, G.; Reining, L.; Rubio, A. Rev Mod Phys 2002, 74, 601.
8. Ehrenreich, H.; Cohen, M. H. Phys Rev 1959, 115, 786; Adler, S. L. Phys Rev 1962, 126, 413; Wiser, N. Phys Rev 1963, 129, 62.
9. Kittel, C. Introduction to Solid State Physics, 6th ed.; Wiley: New York, 1986.
10. Reining, L.; Olevano, V.; Rubio, A.; Onida, G. Phys Rev Lett 2002, 88, 066404.
11. Sottile, F.; Olevano, V.; Reining, L. Phys Rev Lett 2003, 91, 56402.
12. Adragna, G.; Del Sole, R.; Marini, A. Phys Rev B 2003, 68, 165108.
13. Marini, A.; Del Sole, R.; Rubio, A. Phys Rev Lett 2003, 91, 256402.
14. Botti, S.; Sottile, F.; Vast, N.; Olevano, V.; Weissker, H.-C.; Reining, L.; Onida, G.; Rubio, A.; Godby, R. W.; Del Sole, R. Phys Rev B 2004, 69, 115112.
15. Maxwell-Garnett, J. C. Philos Trans R Soc London 1904, A203, 385.
16. Vasiliev, I.; Öğüt, S.; Chelikowsky, J. R. Phys Rev Lett 2001, 86, 1813; Vasiliev, I.; Öğüt, S.; Chelikowsky, J. R. Phys Rev B 2002, 65, 115416 and references therein.

17. Öğüt, S.; Chelikowsky, J. R.; Louie, S. G. Phys Rev Lett 1997, 79, 1770; Öğüt, S.; Chelikowsky, J. R.; Louie, S. G. Phys Rev Lett 1998, 80, 3162.
18. Godby, R. W.; White, I. D. Phys Rev Lett 1998, 80, 3161.
19. Yabana, K.; Bertsch, G. F. Phys Rev B 1996, 54, 4484; Int J Quantum Chem 1999, 75, 55; Rubio, A.; Alonso, J. A.; Blase, X.; Balbás, L. C.; Louie, S. G. Phys Rev Lett 1996, 77, 247; 1996, 77, E5442; Int J Mod Phys B 1997, 11, 2727.
20. Lautenschlagern, P.; Garriga, M.; Viña, L.; Cardona, M. Phys Rev B 1987, 36, 4821.
21. Stiebling, J. Z Phys B 1978, 37, 355.
22. de Heer, W. A. Rev Mod Phys 1993, 65, 611.
23. Brack, M. Rev Mod Phys 1993, 65, 677.
24. Mie, G. Ann Phys (Leipzig) [Folge 4] 1908, 25, 377.
25. Bohigas, O.; Lane, A. M.; Martorell, J. Phys Rep 1979, 51, 267.
26. Brechignac, C.; Cahuzac, Ph.; Leynier, J.; Safarti, A. Phys Rev Lett 1993, 70, 2036; Brechignac, C.; Cahuzac, Ph.; Nebaili, K.; Leynier, J.; Safarti, A. Phys Rev Lett 1993, 68, 3916.
27. Serra, Ll.; Garcias, F.; Barranco, M.; Navarro, J.; Balbás, L. C.; Rubio, A.; Mañanes, A. J Phys Condens Matter 1989, 1, 10391; Phys Rev B 1990, 41, 3434; Z Phys D 1991, 19, 89.
28. Ferrel, T. L.; Echenique, P. M. Phys Rev Lett 1985, 55, 1526.
29. Botti, S.; Vast, N.; Reining, L.; Olevano, V.; Andreani, L. C. Phys Rev Lett 2002, 89, 216803.
30. Botti, S.; Vast, N.; Reining, L.; Olevano, V.; Andreani, L. C. Phys Rev B 2004, 70, 045301.
31. Fiore, A.; Berger, V.; Rosencher, E.; Bravetti, P.; Nagle, J. Nature 1998, 391, 463.
32. Sirenko, A. A.; Etchegoin, P.; Fainstein, A.; Eberl, K.; Cardona, M. Phys Rev B 1999, 60, 8253.
33. Waidmann, S.; Knupfer, M.; Arnold, B.; Fink, J.; Fleszar, A.; Hanke, W. Phys Rev B 2000, 61, 10149; Theory of the Interaction of Swift ions with Matter; Mathar, R. J., Trickey, S. B., Sabin, J. R., Eds.; Advances in Quantum Chemistry 45; Academic Press: London, 2004; Vol. 1, p 277.
34. Marinopoulos, A. G.; Reining, L.; Rubio, A.; Olevano, V. Phys Rev B 2004, 69, 245419.
35. Pichler, T.; Knupfer, M.; Golden, M. S.; Fink, J.; Rinzler, A.; Smalley, R. E. Phys Rev Lett 1998, 80, 4729.
36. Li, Z. M.; Tang, Z. K.; Liu, H. J.; Wang, N.; Chan, C. T.; Saito, R.; Okada, S.; Li, G. D.; Chen, J. S.; Nagasawa, N.; Tsuda, S. Phys Rev Lett 2001, 87, 127401.
37. Marinopoulos, A. G.; Reining, L.; Rubio, A.; Vast, N. Phys Rev Lett 2003, 91, 046402.
38. Spataru, C. D.; Beigi, S. I.; Benedict, L. X.; Louie, S. G. Phys Rev Lett 2004, 92, 077402.
39. Lin, M. F.; Chuu, D. S.; Shung, K. W. K. Phys Rev B 1997, 56, 1430.
40. Delerue, C.; Lannoo, M.; Allan, G. Phys Rev Lett 2000, 84, 2457.
41. Rohlfing, M.; Louie, S. G. Phys Rev Lett 1998, 80, 3320; Grossman, J. C.; Rohlfing, M.; Mitas, L.; Louie, S. G.; Cohen, M. L. Phys Rev Lett 2001, 86, 472.
42. Benedict, L. X.; Puzder, A.; Williamson, A.; Grossman, J. C.; Galli, G.; Klepeis, J. E.; Raty, J-Y.; Pankratov, O. Phys Rev B 2003, 68, 085310.
43. Wagner, L.; Puzder, A.; Williamson, A.; Helms, Z.; Grossman, J. C.; Mitas, L.; Galli, G.; Nayfeh, M. Cond-mat/0403226, 2004, and references therein.
44. Marques, M.; Castro, A.; Rubio, A. J Chem Phys 2001, 115, 3006.
45. Dash, L. K.; Vast, N.; Baranek, Ph.; Cheynet, M. C.; Reining, L. Phys Rev B 2004, 70, 245116.
46. Vast, N.; Reining, L.; Olevano, V.; Schattschneider, P.; Jouffrey, B. Phys Rev Lett 2002, 88, 37601.
47. Aryasetiawan, F.; Gunnarsson, O.; Knupfer, M.; Fink, J. Phys Rev B 1994, 50, 7311.

Appendix: EELS versus ABS, LFE Included

We will assume a compact matrix notation in **G**-space, namely $\chi \equiv \chi_{\mathbf{G},\mathbf{G}'}(\mathbf{q}, \omega)$. Starting from the second of (6) we have

$$\tilde{\chi} = \chi(1 + v\chi)^{-1}$$

that substituted into the first:

$$\begin{aligned}\bar{\chi} &= \chi(1 + v\chi)^{-1} + \chi(1 + v\chi)^{-1}\bar{v}\bar{\chi} \\ &= [(1 + v\chi)\chi^{-1}]^{-1}(1 + \bar{v}\bar{\chi}) \\ &= [\chi^{-1} + v]^{-1}(1 + \bar{v}\bar{\chi}), \quad \text{(A1)}\end{aligned}$$

so

$$[\chi^{-1} + v]\bar{\chi} = (1 + \bar{v}\bar{\chi}) \rightarrow \chi^{-1} + v = \bar{\chi}^{-1} + \bar{v}$$

and

$$\chi^{-1} = \bar{\chi}^{-1} + \bar{v} - v = \bar{\chi}^{-1} - \Delta v$$

$$\chi = [\bar{\chi}^{-1} - \Delta v]^{-1} = \bar{\chi}[1 - \Delta v\bar{\chi}]^{-1}.$$

If we want to consider only the head χ_{00}, we get:

$$\chi_{00} = \sum_{\mathbf{G}_1} = \bar{\chi}_{0\mathbf{G}_1}[(\delta_{\mathbf{G}\mathbf{G}'} - \Delta v_{\mathbf{G}}\bar{\chi}_{\mathbf{G}\mathbf{G}'})^{-1}]_{\mathbf{G}_1 0},$$

where

$$\Delta v_{\mathbf{G}} = \begin{cases} v_0 & \mathbf{G}=0 \\ 0 & \text{else.} \end{cases}$$

Inverting the matrix $(\delta_{\mathbf{G}\mathbf{G}'} - \Delta v_{\mathbf{G}}\bar{\chi}_{\mathbf{G}\mathbf{G}'})$ we can write:

$$\chi_{00} = \frac{\bar{\chi}_{00}}{1 - v_0\bar{\chi}_{00}}.$$

Therefore the difference between χ_{00} and $\bar{\chi}_{00}$ is that the first one is screened. This is important for the discussion in the main text.